CHARACTERISTICS OF FLOWS IN PERVASIVELY FRACTURED ANDESITES, ROTOKAWA GEOTHERMAL FIELD, NEW ZEALAND

Warwick Kissling[1] and Cécile Massiot[1]

[1]GNS Science, 1 Fairway Drive, Avalon, Lower Hutt 5010, New Zealand

w.kissling@gns.cri.nz

ABSTRACT

In New Zealand's high temperature geothermal systems, fluids flow dominantly through fractured rocks with low matrix permeability. It is important to understand the nature of these fracture systems, and how fluids flow through them, so that the geothermal systems may be more efficiently and sustainably used to generate electricity. Here we present fluid flow calculations in several distinct discrete fracture models, each of which is broadly consistent with the fracture density and high dip magnitude angle distributions interpreted from borehole image logs at the Rotokawa Geothermal Field, a New Zealand andesite-hosted reservoir.

Our initial flow calculations are carried out using a cubic flow law, which is derived directly from Darcy's linear relationship between fluid velocity and pressure gradient for flows between smooth parallel plates. For comparison, we then follow with calculations using the Forchheimer flow law, which includes an additional term to account for the friction due to fracture wall roughness.

Most models show pervasive connectivity at reservoir scales, with fluid flow and tracer transport predominantly along the mean fracture orientation. As expected, the models show that permeability anisotropy increases as the standard deviation of the dip distribution decreases, with the fracture system eventually forming into distinct unconnected groups so that across-dip permeability (and hence fluid flow) drops to zero. The models also confirm that significant dispersion of fluid will occur as it is transported through a fractured reservoir. The amount of dispersion shows a broad inverse relation to the permeability anisotropy and reaches a maximum for a uniformly distributed population (unrealistic for Rotokawa) where fracture dip magnitudes vary from horizontal to vertical. Our calculations using the Forchheimer flow law with a subset of the fracture population models show that, as expected, the flow rates drop rapidly as the friction reaches a threshold value and, more surprisingly, the permeability anisotropy decreases at the same time.

1. INTRODUCTION

Fracture networks play an important role in many geothermal systems, where the background rock matrix has extremely low permeability and is therefore not able to support fluid flows necessary to the geothermal industry. Examples of such systems in New Zealand are the greywacke basement-hosted geothermal system at Kawerau (Milicich et al., 2016) and the andesitic lava-hosted system at Rotokawa (McNamara et al., 2016).

In geothermal systems where permeability is controlled by the matrix, or a mixture of matrix and fractures (e.g Ohaaki and Mokai (Bignall et al., 2010)) the behaviour of these reservoirs can be described by 'continuum' models. There,

permeability and other rock properties are ascribed to computational model blocks of size on the order of 10–100 m, and it is assumed that rock properties are constant within each block (e.g. Pruess (1991)). This continuum approach is not so satisfactory when the reservoir permeability is dominated by fractures. In this case, flows can be confined to much smaller 'fracture' length scales (say $\leq$ 1–10 m) while still extending over 'reservoir scale' distances (>100–1000 m) through a connected fracture system (Bonnet et al., 2001). In this situation, it is not possible to accurately represent these structures with a normal continuum-type model without an impractically large number of model elements. An additional complication is that geological measurements of the geometry, permeability and other properties of fractures (e.g. by using borehole image logs) are not sufficient to fully constrain the properties of each fracture, let alone its connectivity with other fractures at reservoir scales. Indeed, while downhole measurements provide in-situ measurements of the fracture systems, some fracture properties such as fracture length cannot be estimated due to the finite diameter of the borehole.

In this paper, we use fracture network statistics derived from downhole and core measurements at the Rotokawa geothermal system (Massiot et al., 2017b), and build on our earlier geometric modelling of fracture networks (Kissling & Massiot, 2017, 2018). We evaluate the effect of the variability of fracture orientation on the fracture network connectivity, permeability, and tracer diffusion at reservoir length scales, quantities which are of interest to reservoir engineers. We present calculations based on both the cubic flow law (e.g Boussinesq, 1868) for smooth-walled fractures and the Forchheimer flow model (e.g. Nield & Bejan (1992); Liu et al. (2016)), which includes an additional term to describe the nonlinear drag (i.e. friction) in real fractures caused by surface roughness of the fracture walls, an effect which is not accounted for by the cubic law.

2. ROTOKAWA FRACTURE NETWORKS

2.1 Context and Applicability

The fracture networks presented here represent the vertical flow through steeply-dipping fractures, as identified based on borehole image logs of the Rotokawa geothermal system. The models and results are also equally applicable to horizontal flow through fracture systems which have a dominant strike orientation (e.g. NE-SW observed throughout the Taupo Volcanic Zone (TVZ) (Massiot et al., 2013; McNamara et al., 2017; Villamor et al., 2017a,b)) and which also occur directly beneath impermeable layers (e.g. the Huka Falls Formation in the TVZ, and in other settings such as the Awibengkok geothermal system in Indonesia (Stimac et al., 2008)).

2.2 Data and Fracture-Network Characterisation

Massiot et al. (2017b) and Kissling & Massiot (2017) describe the basic data sources for the fracture system in

andesitic formations at Rotokawa, the derivation of statistical properties of these networks and geometrical modelling/representation of them. Those previous studies quantified both the connectivity and tendency to form groups of fractures at reservoir scales, assuming a doubly-truncated power-law distribution for fracture length (Bonnet et al., 2001), and furthermore deduced an optimal power-law exponent. A summary of the essential elements of the Rotokawa studies as they pertain to this paper is as follows:

- Image logs from three boreholes sampling >2 km of deviated borehole (mean deviation ~20°) suggest a linear fracture density of 0.55 ± 0.2 m^{-1}.

- Fracture lengths cannot be derived from borehole image logs, but they are assumed to follow a doubly-truncated power law distribution, where the range of fracture lengths is 20−100 m, with a 'best-fit' power-law exponent $\lambda = 2.0$.

- Fracture geometric aperture is set equal to fracture length/1000 for all fractures. This implies that the overall contribution of the fractures to the porosity of the formation (including open fractures and veins) is ~0.05, consistent with that observed in cores, thin-sections and image logs.

- Fracture centres are located by randomly sampling points in the 2D model domain from a uniform distribution.

- A 350 m by 350 m vertical model domain, 100 m in thickness, is used to represent fracturing on a reservoir scale.

- Calculated flows are total volumetric flows through one of the 350 m by 100 m faces of the rectangular model.

The geometric aperture of a fracture derived from borehole image logs or drill-cores is the distance between fracture or vein walls. However, image logs cannot differentiate between open, partially open and closed fractures (Massiot et al., 2017a). In addition, borehole image logs overestimate the geometrical fracture aperture at the borehole walls (Davatzes & Hickman, 2010), and have a resolution (~5 mm) lower than that needed to resolve most fractures observed on cores (<2 mm). Thus, the geometrical fracture aperture used in the models in this paper is significantly greater than the hydraulic aperture which controls the flow of fluids, as presented by e.g. Barton et al. (2013) and Masri et al. (2015). In this paper, we introduce, an additional 'aperture factor' β, which converts from geometric to hydraulic aperture (see section 2.3).

At Rotokawa, most fractures are subvertical, dipping >70°, and statistical analysis of fracture strike and dip magnitude in the three boreholes revealed several populations of fractures with distinct distributions of dip magnitude angle (Massiot et al., 2017b). For simplicity, Kissling and Massiot (2017, 2018) represented the dip magnitudes with a single normal probability distribution where the mean dip is vertical (90°) and the standard deviation 15°. In this study we use five population models for fracture dip angle to explore the effects of dip magnitude variability on the ability of fracture networks to transport fluid. Table 1 (and Figure 1) show

details of these models. In model 1 the dips are represented by a uniform probability distribution between 0° and 180° (i.e., from horizontal to vertical, and dipping in both directions). Models 2, 3 and 4 use single normal distributions with mean 90° and standard deviations of 6°, 15° and 30° respectively for the fracture orientation. The final model, model 5, is based on measured borehole data from Rotokawa which has been corrected for sampling biases (Terzaghi, 1965; Massiot et al., 2015; Massiot et al., 2017), with the fracture dip magnitudes assigned into 10° wide bins between 0° and 180°.
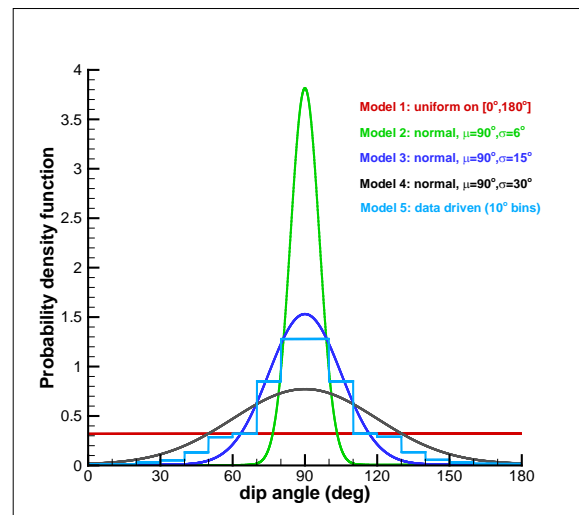

Figure 1: Probability distribution functions for the five fracture dip models studied in his paper. The discrete distribution used in model 5 is derived directly from image log data, and model 3 approximates this using a single normal distribution. Models 1, 2 and 4 are included to provide a comparison with distributions with both larger and smaller variability in the dip angles of the fractures.

2.3 Modelling Approach

Each of the five fracture networks was constructed by sampling from probability distributions for fracture (centre) position, fracture length and fracture dip magnitude (as described in section 2.2). Fractures were added to the model until the target linear fracture density of 0.55 ± 0.2 m^{-1} is reached. As the density of the network increases, the fractures form into groups, which ultimately control the permeability of the model domain. Figure 2 shows a 'realisation', for model 2, which has the specified linear fracture density and forms a single connected group (red fractures) which provides permeable paths across the entire model domain.
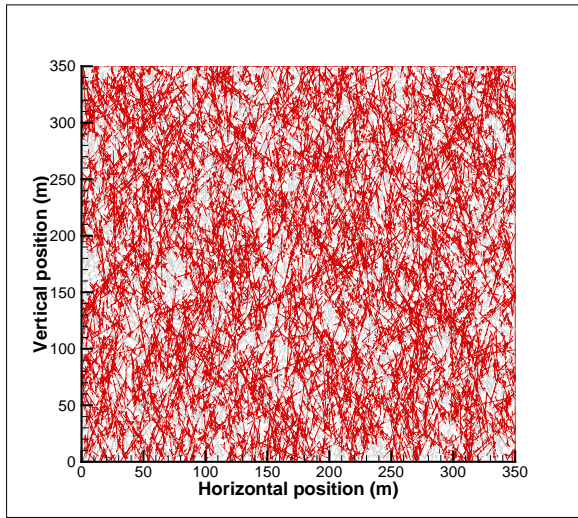
Figure 2: Example of a 'full' fracture network for model 2, where the fracture dip magnitudes are drawn from a normal probability distribution with mean 90° and standard deviation 15°. The red fractures in this network form a single connected group. The remaining grey fractures are isolated and cannot contribute to fluid flows across the model domain.

Typically, with the truncated power law distribution for fracture length, many of the shorter fractures remain unconnected within the network and so cannot contribute to the flow across the model domain (grey background fractures, Figure 2). Similarly, fractures which are connected to only one other (and not to the boundary) are unable to contribute to the overall flow. These unconnected or singly-connected fractures were removed before the calculation of flow across the model. This process is iterative, and results in what is termed the 'backbone network' (or 'backbone' for short, Figure 3), which is the subset of the original network (hereafter the 'full network') which can support flow across the model domain in at least one of the horizontal or vertical directions. Note that the full and backbone networks can contain voids or regions of enhanced fracturing.

The backbone network (or equivalently each of its constituent fully-connected groups if there are more than one) describes the essential connectivity of the fracture network – the locations of all fracture intersections and the properties of the fracture segments connecting them. Locally, the calculation of fluid flow through the fracture system involves calculation of flows in these fracture segments. To do this, two things are required: a) a description of the length, hydraulic aperture and other physical properties of each fracture which govern the flow through it, and b) a mathematical flow law, from which the flow in the fracture segment can be calculated.
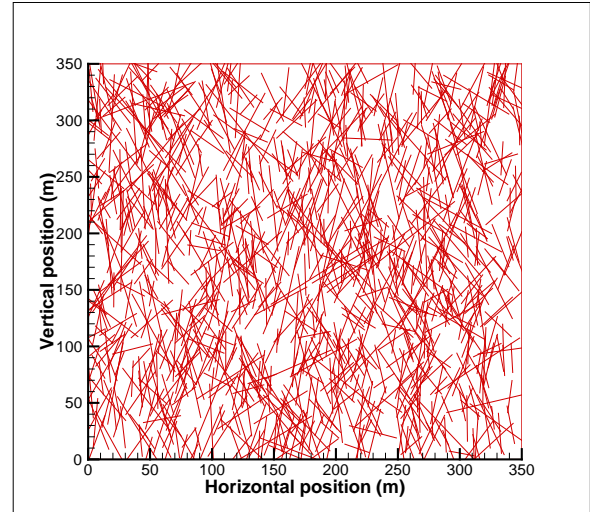

Figure 3: The equivalent 'backbone' for the fracture network shown in Figure 2. The backbone network is obtained by stripping away all unconnected or singly-connected fractures from the full network. This is an iterative process because stripping away fractures can expose further fractures which are either unconnected or singly-connected.

In this paper we use the Forchheimer flow law (Nield & Bejan, 1992) which accounts for 'rough-wall' friction in the fractures:

$$-(k/\mu)\, dP/dL = v + (k^{1/2}\, \rho\, f\, /\, \mu)\, |v|\, v, \quad (1)$$

where k is the permeability, μ the dynamic viscosity, ρ the fluid density, f the non-dimensional Forchheimer coefficient and dP/dL is the pressure gradient along a fracture segment. Then v is the fluid volume flux per unit area of the fracture cross-section. In equation (1), the permeability, k, is given by $(\beta h)^2/12$, where β is the aperture factor (set here to be 0.002 as in Kissling and Massiot (2018)) and h is the geometric aperture of the fracture.

The cubic flow law (Boussinesq, 1868; Zimmerman & Bodvarsson, 1994) is a special case of equation (1), obtained by setting the Forchheimer coefficient f equal to zero. The cubic law describes the flow between smooth-sided parallel plates with a 'no slip' condition on the plates (i.e. the fluid velocity is zero on the fracture walls) and thus is a highly idealised model for flow in real fractures. The additional term in equation (1) accounts for wall roughness and the non-dimensional Forchheimer coefficient is ~1 when this effect is important.

Including the absolute value term |v| in the quadratic term of equation (1) is necessary to ensure that the wall friction always acts to slow the fluid flow for a specified pressure gradient, regardless of its direction. Note also that the quadratic form of the equation implies that v can be found exactly, given dP/dL and other parameters. The condition that the flow law must reduce to the cubic law as the Forchheimer coefficient f tends to zero removes any ambiguity in the choice of the correct root of this quadratic.

On a 'reservoir' scale, the pressure distribution throughout the fracture network determines the flow in each fracture segment. The pressure field is the unknown quantity in the

model and is represented by the pressure at each fracture intersection. Conservation of fluid mass (or equivalently volume, as the model is isothermal) at each fracture intersection implies that the sum of all ingoing and outgoing flows must be zero. This leads to a nonlinear equation involving the pressures at that intersection and each of its nearest neighbours. The complete set of these equations yields a sparse Jacobian matrix with a structure which depends on the connectivity of the backbone network. The individual elements of this matrix are derivatives of the mass conservation equation with respect to pressure at each intersection and the 'right hand side' is simply the mass balance. This system can be readily solved for the pressures at all fracture intersections using a Newton iteration. Lastly, flows through the model domain are calculated by the summing flows for all fracture segments which cross each boundary as described in Kissling & Massiot (2018).

In this paper we also discuss dispersion of fluids and/or tracer particles through the modelled fracture networks. Details of this calculation are given in Kissling & Massiot (2018) and will not be repeated here. For reference however, we show in Figure 4 the possible paths of 1000 distinct fluid particles (in orange) that enter the model domain through the single fracture that is nearest to the centre of the bottom boundary. There are ~20 'exit fractures' on the upper boundary. We define the dispersion of the network as the horizontal spread (i.e. maximum – minimum) that these fractures cover. The dispersion shown in this figure will be referred to as the 'orthogonal dispersion' because it acts to diffuse the fluid orthogonal to the predominant direction of flow (the vertical direction) in the model.
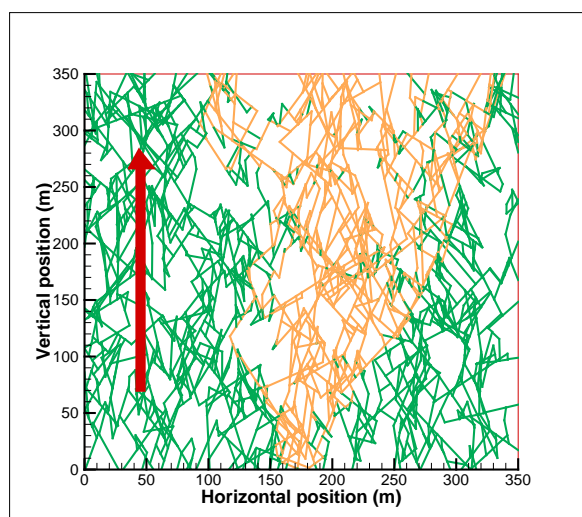

Figure 4: Example of fluid dispersion in a fracture network. The orange fractures trace the paths of 1000 tracer particles. All particles enter the lower boundary through a single fracture (the "entry point") but exit the model domain across approximately 250 m of the upper boundary ("orthogonal dispersion"). The backbone network in this figure does not show any dead-end fracture segments because these do not contribute to the overall flow across the model. The red arrow indicates the direction of the applied pressure gradient.

3. RESULTS AND DISCUSSION

3.1 Simulations

As the geometric properties of individual fracture networks were generated stochastically, we ran ten separate 'realisations' for each of the five models. Each realisation used a different random seed for sampling from the probability distributions for fracture length, fracture position and angle of dip magnitude. These realisations were used to explore the variability of permeability (in the horizontal and vertical directions), permeability anisotropy, and fluid dispersion both within and between each of the models. While the number of realisations was small, it yielded sufficiently well-defined means of quantities such as the flows to afford comparison between the models while still providing useful insight into their inherent variability. In the initial model runs we used the cubic flow law, and then reran some models with the Forchheimer law with a range of Forchheimer coefficients to evaluate what effect it had. In all models a 1 bar pressure difference is applied vertically across the model to drive the flow from bottom to top, For horizontal flows, the same pressure gradient is applied from right to left across the model. Gravity is not included in the calculations as the only effect of this would be to change the effective pressure gradient applied across the model domain. Fluid properties used are calculated at conditions appropriate for Rotokawa geothermal field at ~1 km depth, 100 bar and 320°C.

3.2 Characteristics of Flows: Cubic Flow Law

A basic property of a fracture network is its permeability. We started by using a cubic flow law (equation (1) with f = 0), and the algorithm for calculating flows through the fracture network to measure the equivalent permeability in each direction through the networks, the ratio of these (the permeability anisotropy) and the amount of dispersion of fluid 'particles' due to the variability of flow paths through each network. Results of these calculations for the five models are summarised in Table 1.

Table 1. Summary of flows and derived quantities for the modelled fracture networks, using a Darcy 'cubic' flow law for fracture flow. For model 1, the square brackets [a,b] indicate the range of dip magnitudes of the distribution. Unbracketed entries elsewhere in the table indicate: mean ± 1 standard deviation derived from the ten independent realisations of each model.

Model	Orientation probability density function	Flow along-dip (vertical) (m^3s^{-1} x 1000)	Flow across-dip (horizontal) (m^3s^{-1} x 1000)	Permeability anisotropy (across/along)	Orthogonal Dispersion (m at Y=350 m)
1	Uniform: [0°, 180°]	1.21 ± 0.23	1.11 ± 0.17	1.10 ± 0.18	259 ± 61
2	Normal: (μ=90°, σ=6°)	0.35 ± 0.18	0.007 ± 0.009	>20	< 61
3	Normal: (μ=90°, σ=15°)	2.67 ± 0.52	0.28 ± 0.08	10.0 ± 2.5	117 ± 41
4	Normal: (μ=90°, σ=30°)	2.29 ± 0.32	0.65 ± 0.14	3.6 ± 0.7	183 ± 45
5	Data-driven (μ=90°, σ=20°, measured)	2.44 ± 0.40	0.30 ± 0 .06	8.3 ± 1.8	141 ± 43

Starting with model 1 (isotropic fracture orientation), the permeability anisotropy is consistent with unity within less than one standard deviation, as expected for a network where every orientation of fracture is equally likely.

Of the three 'normal distribution' models (2, 3 and 4) the most obvious feature is the small vertical flow for model 2 and the corresponding horizontal flow, which is very small and indeed consistent with zero. The reason for this is that the small standard deviation of fracture dips in this model (6°) limits the lateral 'reach' of fractures, and hence the connectivity of the network in the direction orthogonal to the mean fracture dip. As a result, realisations of this model show a tendency for channelling, with one or more separate and mutually unconnected groups of fractures providing good along-dip (vertical) permeability but no across-dip (horizontal) connectivity. An extreme example of this channelling, with six groups, is shown in Figure 5.

Because each of the groups in Figure 5 connects the upper and lower boundaries of the model domain, there is clearly some permeability in the vertical direction. However, the sum of the vertical flows over the six groups in this model (see Table 1) is only ~10% of those in models 3, 4 and 5, suggesting the permeability in each of the groups is much reduced compared to those models. This effect is attributed generally to the fact that the backbone networks in model 2 contain fewer fractures than the other models, and with smaller directional variability, and that within each fracture group there are a limited number of pathways for fluid to be transported across the model domain.

For models 3 and 4, as the standard deviation of the fracture dip magnitude increases the across mean dip flow (or equivalently, the permeability) also increases (Table 1) and there is sufficient connectivity for all fractures in the backbone network to form a single connected group. Although the vertical-direction flows are of similar magnitude in models 3 and 4, there is a clear increase in the horizontal flow associated with the larger dip standard

deviation in model 4. The permeability anisotropy for this model is, therefore, much reduced compared to model 3. Even higher dip magnitude standard deviations (above 30°) reduce the permeability anisotropy further, and at some critical dip standard deviation this creates a network with essentially isotropic permeability similar to model 1. A preliminary investigation shows that this occurs for dip standard deviations in the range ~60°–70° and that the four properties we are considering (the horizontal and vertical flows, their ratio and the fluid dispersion) are at that point very similar (within a few percent) to those of model 1.

The average properties of the data-driven model 5 (Table 1) all lie between the corresponding entries for models 3 and 4. This suggests that the ability of the intermediate to low angled fractures (dip magnitudes less than 60° with either dip direction) in this model to provide horizontal (and vertical) connectivity might be mimicked with a normal distribution with a suitably fine-tuned standard deviation between those of models 3 and 4, i.e., between 15° and 30°. However, unlike the uniform distribution of fracture dips in model 1, no single model using a normal distribution can be found which is completely consistent with the data-driven model 5. Either the flows/anisotropy can be matched but not the fluid dispersion, or vice-versa, but not both. This shows that fractures in the heavy tails of the data-driven dip magnitude angle distribution (Figure 1) provide greater lateral connectivity than is possible with any normally distributed model.

The orthogonal dispersion is largest for model 1, and smallest for model 2 which has the smallest spread of fracture dip magnitudes (Table 1). For model 2 the orthogonal dispersion can technically be zero as we have defined it (section 2.3) because the fluid paths are geometrically limited by the finite horizontal width of the fracture groups (Figure 5), and in some groups only a single exit fracture exists.
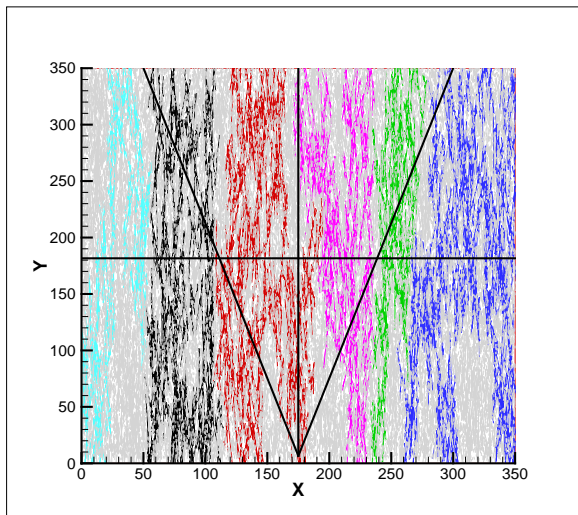
Figure 5: Distinct fracture groups in model 2 (normally distributed dips, μ=90°, σ=6°). Colours indicate distinct unconnected groups of fractures. Grey indicates 'background' fracturing which does not provide connected permeability across the model. This fracture network provides good permeability in the vertical direction (though reduced compared to the other models which are connected across the domain), but zero permeability in the horizontal direction.

3.3 Characteristics of Flows: Forchheimer Flow Law

The results in section 3.2 were calculated using a cubic flow law (Equation (1) with the Forchheimer coefficient f=0). In this section the calculations are repeated for some models with the Forchheimer term included to investigate how the properties of the flows might be affected.

For model 1, as expected when including a frictional term in the flow equation, the magnitude of the flows (either X- or Y- directions) decreases as the friction increases, the effect becoming apparent for a Forchheimer coefficient greater than ~10^{-4} (Figure 6). Because model 1 has no preferred fracture direction, a necessary requirement for this model is that the permeability anisotropy remains close to one over the full range of Forchheimer coefficients examined, < ~2. This is confirmed by the blue curve in Figure 6. The standard deviation of the anisotropy varies over the range ~0.12-0.17 and is not shown to avoid clutter in the figure. Intriguingly, the orthogonal fluid dispersion in this model (and that in models 3 and 5) grows modestly, with some fluctuations, for Forchheimer coefficient greater than ~0.5, but it is not yet clear if this is a real physical effect or a statistical fluctuation which would disappear if more model realisations were used to calculate the average dispersion.

Figure 7 shows how the vertical flows and permeability anisotropy for models 1, 3 and 5 vary as a function of Forchheimer coefficient. The decline in flows as the frictional term grows is apparent (and expected) for these models. Less obviously, the flows decline preferentially most in the larger fractures, say longer than 50–60 m, which provide most of the capacity of the fracture network to support fluid flow. This bias explains why the permeability anisotropy for models 3 and 5 also decreases as the friction increases—there are more large fractures providing (vertical direction) flow through the lower and upper boundaries of the model than there are providing flows through the lateral

boundaries. In model 1 this effect does not occur because there are statistically equal numbers of large fractures crossing the boundaries in both directions.
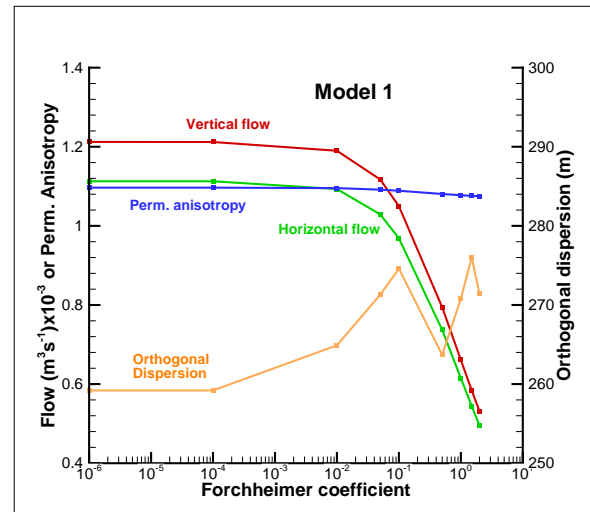

Figure 6: Properties of model 1 with the Forchheimer term included. Because of the frictional term, the magnitude of the flows decreases as the Forchheimer coefficient increases, and, for this model, the permeability anisotropy (blue) remains close to one. Each data point represents the average derived from ten separate simulations for each Forchheimer coefficient.
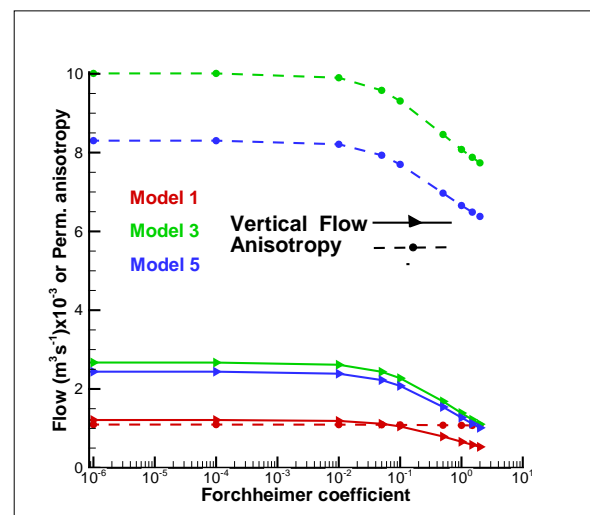

Figure 7: Permeability anisotropy and vertical direction flow for models 1, 3 and 5 as a function of Forchheimer coefficient. The effect of the Forchheimer (frictional) term becomes apparent at f = ~0.01 where the curves turn down. The permeability anisotropy for model 1 is consistent with one. Each data point represents the average derived from ten separate simulations for each Forchheimer coefficient.

In general, fluid dispersion will vary with the direction of the applied pressure gradient. In the calculations described so far the mean fracture direction (except for model 1) was aligned with the pressure gradient, but our models also allow the dispersion to be calculated when the pressure gradient is applied across the mean fracture direction. This is referred to as the cross-dispersion. Figure 8 shows both the orthogonal and cross dispersions for models 1, 3 and 5 as a function of Forchheimer coefficient. For model 1, with a uniform distribution of fracture dips, we expect that the orthogonal and cross dispersions will be 'statistically' similar with a ratio close to one, and this is confirmed in Figure 8. Models 3 and 5 have similar orthogonal dispersions which are both significantly lower than that for model 1. However, models 1 and 5 have similar cross dispersions, which are both higher than that of models 3. These characteristics of fluid dispersion in 2D as a function of the fracture orientations are relevant to the interpretation of tracer tests.
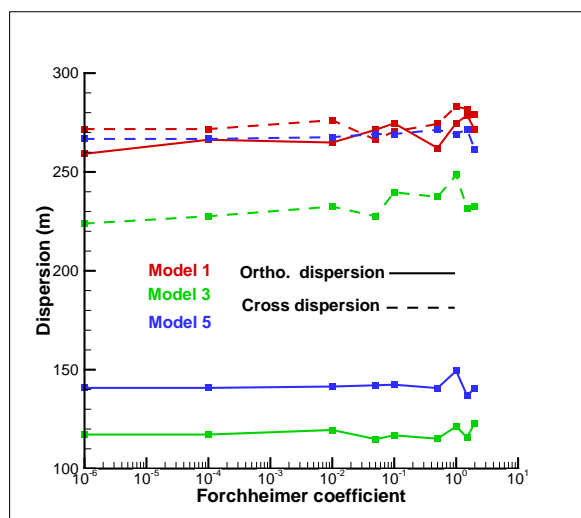

Figure 8: Fluid dispersion in two directions for models 1, 3 and 5 as a function of Forchheimer coefficient. Each data point represents the average derived from ten separate simulations for each Forchheimer coefficient.

3.4 From Fracture Models to Continuum Models

Ultimately, the purpose of this work is to provide a better description of the flow through fractured rock that can be used to improve the understanding and management of the Rotokawa geothermal field and other TVZ systems. This will require melding results such as those calculated in this paper with more traditional continuum approaches to modelling geothermal systems for engineering purposes (e.g. Pruess, 1991).

A good recent example of this is contained in Hadgu et al., (2017), who compare modelling of flow through a 1 km^3 cube of fractured block containing approximately 6500 fractures, using both discrete fracture network (DFN) and equivalent continuum modelling (ECM) approaches. The context of their work is the flow of water in the region of a high-level nuclear waste repository, but the methods and results are equally applicable to modelling a geothermal system. The two modelling approaches are used to compare (a) the bulk permeabilities (in 3D) and (b) the breakthrough curves for transport of a non-reactive tracer through the model domain.

Both of these represent important information for reservoir engineers and modellers. Kissling and Massiot (2018) performed similar calculations for 2D models of the fractured andesites at Rotokawa, and so, at least in principle, these are easily extendable to a full 3D engineering model of the Rotokawa system.

The dispersion of fluid (or, equivalently, non-reacting tracers) by fracture networks is not discussed in Hadgu et al., (2017) but is an important aspect of the fluid transport in geothermal systems which has hitherto been ignored by continuum modellers. Zhao et al., (2010) present a method for estimating the components of the hydrodynamic dispersion matrix of a fracture network which might be implemented in a continuum model. Their method is based on 'random-walk' tracing of fluid paths and can be implemented using the particle tracing techniques we have described in Kissling and Massiot (2018).

While the three borehole image logs, representing 2.1 km of borehole length, provide invaluable direct measurement of fractures in the Rotokawa andesites, they still sample a small part of the entire rock volume. In addition, variations in fracture orientations are observed within and between boreholes. The problem of describing the flow through these formations is thus inherently a statistical one. Multiple realisations of fracture networks with the same target linear fracture density are required to determine realistic probability distribution functions (PDFs) for the quantities calculated in this paper – the components of permeability and dispersion in 2D, and the permeability anisotropy. This work has already begun, with a parallel version of our code now tested and able to process approximately 2500 realisations (of the 350 m by 350 m model described here) per day, including tracing 1000 particle paths for each network. Continuum reservoir scale models populated with such PDFs will produce a range of possible predictions within which the measured reservoir changes should necessarily fall. Should this not happen, recalibration of the model will be needed. This process will be computationally challenging but should result in more robust modelling and management of the geothermal resource.

4. CONCLUSIONS

We have presented five different models for studying the effects of fracture dip magnitude on fluid flow. Two of these models represent fracture dip magnitude data measured in-situ in andesites of the Rotokawa Geothermal Field. The remaining three models are used for comparison. Individual models were populated with fractures based on probability distributions for fracture length, fracture location within the model domain and fracture orientation. We calculated flows across a 'reservoir-scale' region using these fracture models. Flow calculations were performed using a 'cubic flow' law and its extension using a frictional Forchheimer term. All flow calculations were both isothermal and steady state, and the paths of the tracer particles generated using the using the steady state fluid velocities and the probabilistic method described in Kissling and Massiot (2018). The variability of permeabilities (in 2D), the permeability anisotropy and the tendency of the fracture networks to disperse fluid (again in two dimensions) were explored using these flows.

A uniform distribution for dip angles is unrealistic for Rotokawa, but calculated values of the permeability anisotropy and the ratio of orthogonal to cross dispersions for the uniformly distributed network is consistent with the

expected value of unity within statistical uncertainties. This provides a valuable 'sanity check' for our methods. We confirm that a model with normally distributed dip magnitude angles and a low standard deviation for dip angles indeed shows channelling of the permeability and is not able to provide continuous connectivity perpendicular to the mean fracture direction. We determine that the threshold for this to occur lies at a standard deviation of 6°. Models with larger standard deviations will provide good permeability in both along-dip and across-dip directions. This threshold could be used as an indicator of permeability channelling in future image log interpretations where the linear fracture density is similar to that described in this paper.

All models are found to disperse fluid (or tracer particles), and the magnitude of this effect is inversely related to the permeability anisotropy of the network. The dispersion also depends on the direction of the applied pressure gradient relative to the mean fracture dip magnitude, with further variations depending on the standard deviation of fracture dip magnitude.

While the cubic flow law is used most commonly in studies of fracture flow, we have also used the nonlinear Forchheimer model, which includes additional frictional term due to the fracture wall roughness and is more geologically realistic. This reduces the flows across all models compared to the cubic model, and hence the equivalent permeability of the fracture networks. Our models also show, surprisingly, that the permeability anisotropy decreases in all models as the Forchheimer term increases. The exception to this is where the fracture dip magnitudes are described by a uniform distribution. In this case, as expected, the permeability anisotropy remains consistent with unity to within the statistical uncertainties.

The Rotokawa 'data-driven' model 5 is best represented by the single normal distribution with an intermediate standard deviation of 15°, as expected from the natural distribution of observed fractures, but this simple model cannot capture both the permeability and the dispersion resulting from the data-driven model at the same time. Ultimately our aim is to use these fracture population models to inform more traditional continuum models of the Rotokawa geothermal system, with the hope that they will provide a better description of fluid flow within the reservoir and aid the responsible and sustainable use of that resource in the future.

ACKNOWLEDGEMENTS

REFERENCES

Barton, C. A., Moos, D., Hartley, L., Baxter, S., Foulquier, L., Holl, H., & Hogarth, R. (2013). Geomechanically coupled simulation of flow in fractured reservoirs. *Proc. of the 38th Workshop on Geothermal Reservoir Engineering, Stanford.*

Bignall, G., Rae, A. J., & Rosenberg, M. D. (2010). Rationale for targeting fault versus formation-hosted permeability in high-temperature geothermal systems of the Taupo Volcanic Zone, New Zealand. *Proc. World Geothermal Congress.*

Bonnet, E., Bour, O., Odling, N. E., Davy, P., Main, I., Cowie, P. A., & Berkowitz, B. (2001). Scaling of fracture systems in geological media. *Reviews of Geophysics*, **39**(3), 347–383. doi: 10.1029/1999RG000074

Boussinesq, J. (1868). Memoire sur l'influences des frottements dans les movements reguliers des fluids. *Journal de Mathématiques Pures et Appliqués*, 13, 377–424.

Davatzes, N. C., & Hickman, S. H. (2010). Stress, fracture, and fluid-flow analysis using acoustic and electrical image logs in hot fractured granites of the Coso Geothermal Field, California, U.S.A. In M. Poppelreiter, C. Garcia-Carballido, & M. Kraaijveld (Eds.), Dipmeter and borehole image log technology: AAPG Memoir 92 (pp. 259–293). doi:10.1306/13181288M923134

Hadgu, T., Karra, S., Kalinina, E., Makedonska, N., Hyman, J., Klise, K., Viswanathan, H., & Wang, Y. (2017). A comparative study of discrete fracture network and equivalent continuum models for simulating flow and transport in the far field of a hypothetical nuclear waste repository in crystalline host rock. *Journal of Hydrology*, 553, 59-70.

Kissling, W. M., & Massiot, C. (2017). Geometric modelling of fracture networks in an Andesite-hosted geothermal reservoir. *Proc. 39th New Zealand Geothermal Workshop.*

Kissling, W. M., & Massiot, C. (2018). Modelling flows in discrete fracture networks derived from a New Zealand lava-hosted geothermal system. *Proc. 40th New Zealand Geothermal Workshop.*

Liu, R., Li, B. and Jiang, Y. (2016). Critical hydraulic gradient for nonlinear flow through rock fracture networks: The roles of aperture, surface roughness, and number of intersections. *Advances in Water Research,* 88, 53-65.

Masri, A., Barton, C. A., Hartley, L., & Ramadhan, Y. (2015). Structural Permeability Assessment Using Geological Structural Model Integrated with 3D Geomechanical Study and Discrete Facture Network Model in Wayang Windu Geothermal Field, West Java, Indonesia. *Proc. 40th Workshop on Geothermal Reservoir Engineering, Stanford.*

Massiot, C., McNamara, D. D., Lewis, B. (2013). Interpretive review of the acoustic borehole image logs acquired to date in the Wairakei-Tauhara Geothermal Field. GNS Science report 2013/04.

Massiot, C., McNamara, D. D., & Lewis, B. (2015). Processing and analysis of high temperature geothermal acoustic borehole image logs in the Taupo Volcanic Zone, New Zealand. *Geothermics*, 53, 190–201. doi: 10.1016/j.geothermics.2014.05.0107

Massiot, C., McLean, K., McNamara, D. D., Sepulveda, F., & Milicich, S. D. (2017a). Discussion Between a Reservoir Engineer and a Geologist: Permeability Identification from Completion Test Data and Borehole Image Logs Integration. *Proc. 39th New Zealand Geothermal Workshop.*

Massiot, C., Townend, J., Nicol, A., & McNamara, D. D. (2017b). Statistical methods of fracture characterisation

using acoustic borehole televiewer log interpretation. *Journal of Geophysical Research*, 122(8), 6836–6852. doi: 10.1002/2017JB014115

McNamara, D. D., Massiot, C., & Milicich, S. M. (2017). Characterizing the subsurface structure and stress of New Zealand's geothermal fields using borehole images. *Energy Procedia*, 125, 273–282.

McNamara, D. D., Sewell, S. M., Buscarlet, E., & Wallis, I. C. (2016). A review of the Rotokawa Geothermal Field, New Zealand. *Geothermics*, 59, 281–293. doi: 10.1016/j.geothermics.2015.07.007

Milicich, S. D., Clark, J. P., Wong, C., & Askari, M. (2016). A review of the Kawerau Geothermal Field, New Zealand. *Geothermics*, 59, 252–265. doi: 10.1016/j.geothermics.2015.06.012

Nield, D. A., & Bejan, A. (1992). Convection in Porous Media. Springer Verlag, New York.

Pruess, K. (1991). TOUGH2 – A General-Purpose Numerical Simulator for Multiphase Fluid and Heat Flow. Lawrence Berkeley Laboratory Report LBL-29400.

Stimac, J., Nordquist, G., Suminar, A., & Sirad-Azwar, L. (2008). An overview of the Awibengkok geothermal system, Indonesia. *Geothermics*, 37, 300–331. doi: 10.1016/j.geothermics.2008.04.004

Terzaghi, R. D. (1965). Sources of error in joint surveys. *Geotechnique*, 15(3), 287–304. doi: 10.1680/geot.1965.15.3.287

Villamor, P., Berryman, K. R., Ellis, S. E., Schreurs, G., Wallace, L. M., Leonard, G. S., Langridge, R. M., & Ries, W. F. (2017a). Rapid evolution of subduction-related continental intra-arc rifts: The Taupo Rift, New Zealand. *Tectonics*, 36, 2250–2272.

Villamor, P., Nicol, A., Seebeck, H. C., Rowland, J. V., Townsend, D., Massiot, C., McNamara, D. D., Milicich, S. D., & Alcaraz, S. (2017b). Tectonic structure and permeability in the Taupō rift: New insights from analysis of Lidar derived DEMs. *Proc. 39th New Zealand Geothermal Workshop.*

Zhao, Z., Jing, L., & Neretnieks, I. (2010). Evaluation of hydrodynamic dispersion parameters in fractured rocks. *Journal of Rock Mechanics and Geotechnical Engineering*, 2(3), 243-254.

Zimmerman, R. W., & Bodvarsson, G. S. (1994). Hydraulic Conductivity of Rock Fractures. Lawrence Berkeley Laboratory Report LBL-35976.